Nuclear Instruments and Methods in Physics Research A 1056 (2023) 168646

Contents lists available at ScienceDirect

Nuclear Inst. and Methods in Physics Research, A

journal homepage: www.elsevier.com/locate/nima

Full Length Article

Upgrade of the MARI spectrometer at ISIS

M.D. Le [a,*], T. Guidi [a,b], R. Bewley [a], J.R. Stewart [a], E.M. Schooneveld [a], D. Raspino [a], D.E. Pooley [a], J. Boxall [a], K.F. Gascoyne [a], N.J. Rhodes [a], S.R. Moorby [a], D.J. Templeman [a], L.C. Afford [a], S.P. Waller [a], D. Zacek [a], R.C.R. Shaw [a]

[a] *ISIS Neutron and Muon Source, STFC Rutherford Appleton Laboratory, Harwell Campus, Didcot OX11 0QX, United Kingdom*
[b] *Physics Division, School of Science and Technology, University of Camerino, 62032 Camerino, Italy*

ARTICLE INFO

Keywords:
Neutron instrumentation
Inelastic neutron spectroscopy
Time-of-flight spectroscopy

ABSTRACT

The MARI direct geometry time-of-flight neutron spectrometer at ISIS has been upgraded with an $m = 3$ supermirror guide and new detector electronics. This has resulted in a flux gain of $\approx 6\times$ at $\lambda = 1.8$ Å, and improvements on discriminating electrical noise, allowing MARI to continue to deliver a high quality science program well into its fourth decade of life.

1. Introduction

MARI is a time-of-flight direct-geometry spectrometer located in the first target station at the ISIS Neutron and Muon Spallation Source, Rutherford Appleton Laboratory, UK. It was amongst the first instruments designed and built at the early days of ISIS [1,2], and was funded as part of the UK-Japan collaboration initiated by the late Professor Yoshikazu Ishikawa. The instrument was named MARI (真理) in honor of Prof. Ishikawa's daughter, and means "Truth" in Japanese. It was completed and started user experiments at the end of 1989. Its original design complemented the highly successful HET (High Energy Transfer) spectrometer by increasing the detector coverage and having a peak flux at lower energies (at ≈25 meV) provided by the 110 K liquid methane moderator. The 4 m secondary flight path (sample-detector distance) also ensures a good energy resolution, which can be as fine as 1% of the incident energy. MARI also has a unique vertical scattering geometry where the detectors are mostly below the sample position. This gives it an extremely low background count rate of approximately 6 counts per hour per meter of detector, due to the increased shielding below the target compared to that in the horizontal plane.

The wide scattering angle range (≈ 5–135°) covered by the MARI detectors[1] has allowed many different types of scientific problems to be addressed by the instrument on polycrystalline and liquid samples in its first two decades of operation. While initially focused on measurements of phonon density of states (PDOS) in crystalline solids, liquids and amorphous materials, over time the science program has shifted towards the study of magnetic excitations, to the point that around two-thirds of the beam time is currently devoted to magnetic materials.

Despite this past success, by modern standards MARI's incident flux was too low to be competitive, as it possessed no neutron guide. It was thus recently upgraded with an $m = 3$ straight converging neutron supermirror guide which has increased its flux by a factor of 6 at 25 meV (1.8 Å), where the peak flux is. This gain is larger at lower energies. In addition to the new guide, MARI has also had a new double-disk chopper installed to allow greater flexibility in the use of replication rate multiplication (RRM), and the detector and data acquisition electronics were also upgraded, allowing better signal processing and improved event-mode data collection.

With several years of user operation since the upgrade, the improved performance of MARI has enabled experiments to be carried out faster and for previously unfeasible experiments to be completed. This has allowed MARI to make contributions in a variety of science areas from thermoelectric and battery materials to superconductivity and low dimensional magnetism.

We first describe the original MARI (Section 2), then detail the guide (Section 3), choppers (Section 4) and detector electronics (Section 5) upgrades. Finally, we evaluate the performance of the upgraded instrument (Section 6) and showcase recent scientific examples (Section 7).

2. MARI original design

The pre-upgrade layout of the MARI primary spectrometer [1,2] is shown schematically in Fig. 1(a), and consists of evacuated square

---

* Corresponding author.
E-mail address: duc.le@stfc.ac.uk (M.D. Le).

[1] MARI has 1 inch by 1 foot non-position sensitive detectors positioned so that three tubes cover the same scattering angle (2θ) in a Debye–Scherrer geometry. This means the detector bank is approximate 1 m wide.

https://doi.org/10.1016/j.nima.2023.168646
Received 18 November 2022; Received in revised form 14 August 2023; Accepted 26 August 2023

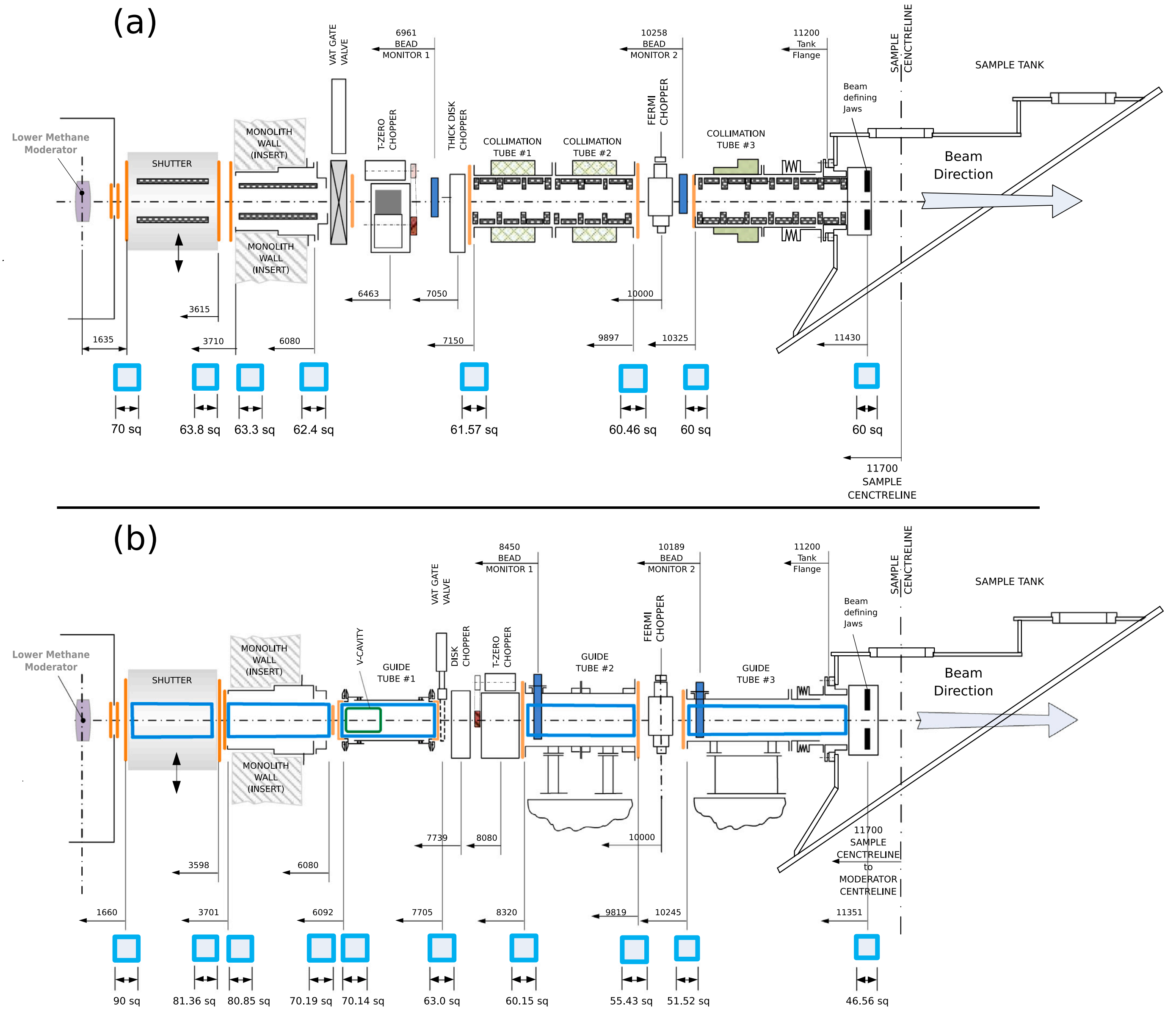

Fig. 1. Schematic of (a) the old and (b) the new designs of the MARI spectrometer. Blue squares below each schematic indicate the cross-section size of the beam at that point. All measurements are in millimeters and distances are specified with respects to the moderator center unless otherwise stated.

cross-sectioned beam tubes lined with neutron-absorbing boron carbide (B_4C) together with three choppers: A T0 chopper made from Nimonic alloy at 6.4 m from the moderator, to stop fast neutrons; A thick disk chopper with a single slot at 7.0 m to transmit a single neutron pulse for each proton pulse and hence reduce background and a monochromating fast Fermi chopper at 10 m. However, this precludes the use of the repetition-rate multiplication (RRM) technique to improve the efficiency of the measurements as described in Section 4.

There is a beam monitor (M1) before the disk chopper which can be used to normalize the data. A second monitor after the Fermi chopper (M2), together with a final monitor in the “get-lost” tube before the beam stop (M3, not shown) is used to determine the energy of the neutrons incident on the sample. All beam monitors use lithium-6 glass beads scintillators.

Finally, the sample tank is shown which may be pumped down to a cryogenic vacuum ($\approx 10^{-7}$ mBar), whilst the detectors (not shown) form an arc *below* the sample covering scattering angles from −15° to +135°, at a sample-detector distance of 4 m.

3. Guide upgrade

The new $m = 3$ converging guide is installed in 5 sections, shown schematically as blue rectangles in Fig. 1(b). The first section is embedded in a new evacuated shutter, and the second section is mounted in an insert tube in the target station monolith shielding. Sections 3–5 are outside the monolith and are separated by two pits, the first containing the disk and Nimonic (T0) choppers and the second with the fast Fermi chopper. These guide sections have also been fitted with inclinometers to monitor, via a control box and software, the guide alignment over time. One packaged unit is screwed to the outside of each guide’s vacuum housing plus an internal unpackaged unit on each internal glass section. The new Fermi chopper is mounted on a lift and can be moved out of the beam for white beam measurements without manually removing the chopper as was the case before the upgrade.

The guide design is a rather conservative one, chosen mainly for ease of manufacturing and installation as the upgrade project had to be completed within a short window timed with a long shut down period of the accelerator. Nonetheless, the guide design gives a brilliance

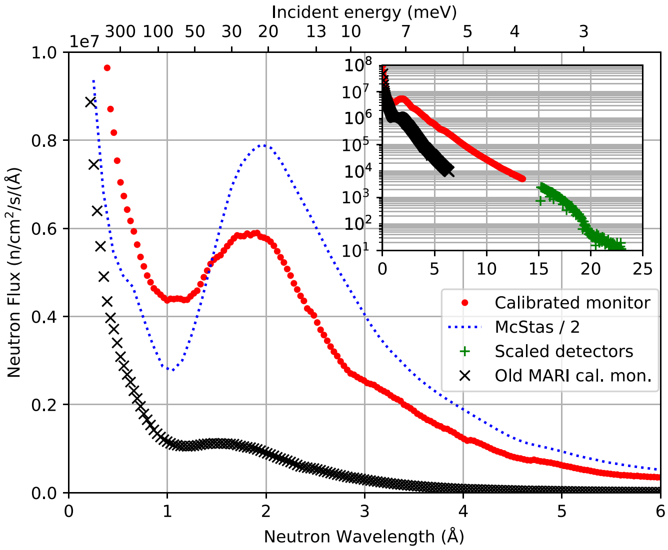

Fig. 2. Measured (circles) and calculated (dotted line) white beam flux at the sample position of upgraded MARI normalized to a nominal proton beam current of 175 μA. The inset shows an expanded spectra with supplementary measurements up to 23 Å using the low angle detectors (crosses) as described in the text to illustrate the attenuation cut-off around 19 Å due to the V-cavity frame overlap mirror.

transfer [3] of 49% for a sample size of 40 × 40 mm, divergence of 2° and wavelength range between 1 and 10 Å, as calculated from McStas. The brilliance transfer could be improved by increasing the guide m value, or reducing the sample size. However, increasing m above 3 was considered too expensive and time-consuming, whilst reducing the sample size (increasing the guide focus) would have reduced the flexibility to measure large or absorbing samples.

Whilst the Fermi chopper position remains the same (10 m from the moderator), the disk and Nimonic choppers were moved closer to the sample so as to reduce the possibility of radiation damage. In previous operations, it was found that the motor encoders on these choppers needed to be replaced every 1–2 years. In addition, due to space constraints and in order to minimize air gaps between components, the new double disk chopper is placed *before* the Nimonic chopper, and the first monitor (M1) is placed in Guide 4 after the disk and Nimonic. As MARI now often runs with the Gd chopper and so must use the disk, this monitor no longer records the white beam incident spectrum. This monitor and the monitor (M2) after the Fermi chopper are placed in vacuum inside guides 4 and 5 respectively. Both monitors use lithium-6 glass beads in a similar design to the pre-upgrade monitors but with fewer beads as the incident flux is now greater.

The initial opening and view of the methane moderator is 90×90 mm, and this converges down to a view of 45×45 mm at the sample position, compared with the pre-upgrade cross-sections of 70×70 mm at the moderator end and 60×60 mm at the sample end. The new larger view of the moderator gives a 1.65× gain at all energies, whereas the gain from the guide itself is neutron wavelength dependent, approaching unity at short wavelengths (high energies). Section 3 also has a single 200 mm long V-cavity frame-overlap mirror (FOM), consisting of two $m = 5$ supermirrors on a Si substrate at a taper of 9°, designed to scatter neutrons with wavelength longer than ≈20 Å out of the beam. The inset to Fig. 2 shows the long wavelength flux (green crosses), and the reduction due to the FOM around 20 Å. These measurements were made with the disk chopper running at 10 Hz (without the Fermi chopper) and uses the low angle (3.5°) detectors, as these neutrons are very divergent (≈ 5°) so they impinge directly on the low angle detectors. This fact, however, makes the low angle detectors unusable in normal operation, where we find that we need to mask detectors below ≈ 6°.

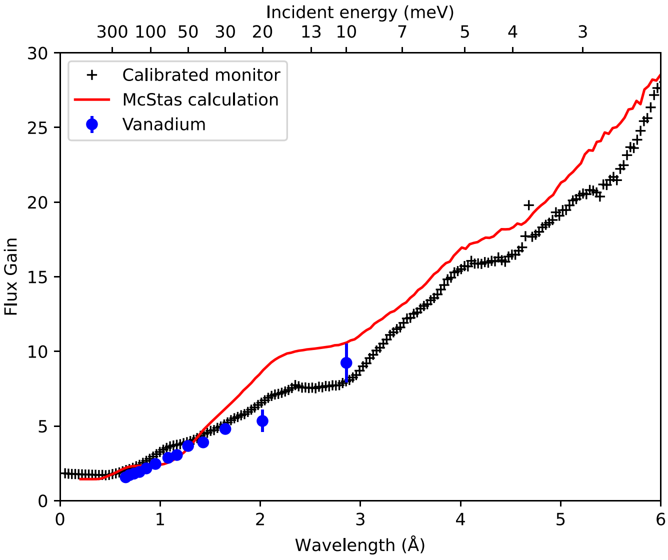

Fig. 3. Gains from the new guide on MARI. Crosses show measurements with a calibrated monitor and circles are integrated scattered intensities from a Vanadium standard sample with the Gd chopper, averaged over runs with different frequencies at the same incident energy. The solid line is calculated from McStas simulations.

Fig. 2 shows the measured and calculated absolute flux of the upgraded MARI instrument and Fig. 3 shows the measured and calculated gains from the guide. The measurements, taken in 2016 before and in 2018 after the guide upgrade, used the same calibrated GS1 glass scintillating bead monitor [4] mounted at the sample position, giving an absolute flux measurement, and the gain was obtained by the ratio of the two results. Likewise, the calculated gain was obtained from the ratio of the calculated flux from McStas [5] simulations of the pre- and post-upgrade instrument. The calculated flux in Fig. 2 is shown scaled down by a factor of 2, which from our experience is necessary due to inaccuracies in the moderator models, based on MCNPX calculations [6], used for ISIS instruments.

The measured and calculated flux gain is displayed in Fig. 3, showing that around the peak flux ($\approx$ 1.8 Å) the flux gain from the upgrade is a factor of 6, and this increases with longer incident neutron wavelengths: At the lowest commonly used incident wavelength λ = 3.7 Å (incident energy E_i = 6 meV), the flux gain is a factor of 14. This has made low energy measurements more feasible than before the upgrade. Test measurements were also made with λ = 6.4 Å (E_i = 2 meV) where the gain is a factor of 30 but even so the flux is too low to be usable except with a large sample.

The flat plateaus in the gain are due to the gaps in the guide to accommodate the disk/Nimonic and Fermi chopper pits, which means that neutrons which would have been reflected by a guide there are lost. These gaps also cause a slight non-uniformity in the beam profile for longer wavelengths, as shown in Fig. 4, where a dip in flux in the center of the beam can be seen for a representative case of λ = 3.3 Å. The full dataset of beam profiles for wavelengths from 1 to 10 Å is included in the supplementary materials. The beam profile was measured using a 2D time-sensitive neutron gas electron multiplier (nGEM) detector [7] at the sample position with an active area of 100×100 mm and pixel size of 0.8 mm (128×128 pixels). Scaled McStas simulations integrated over the same time-of-flight ranges show good agreement with the measurements, as shown in Fig. 4. The slightly non-uniform beam profile may result in a non-analytic resolution profile, and work is progressing to include a ray-tracing element to the resolution calculations used in standard analysis programs like Horace [8].

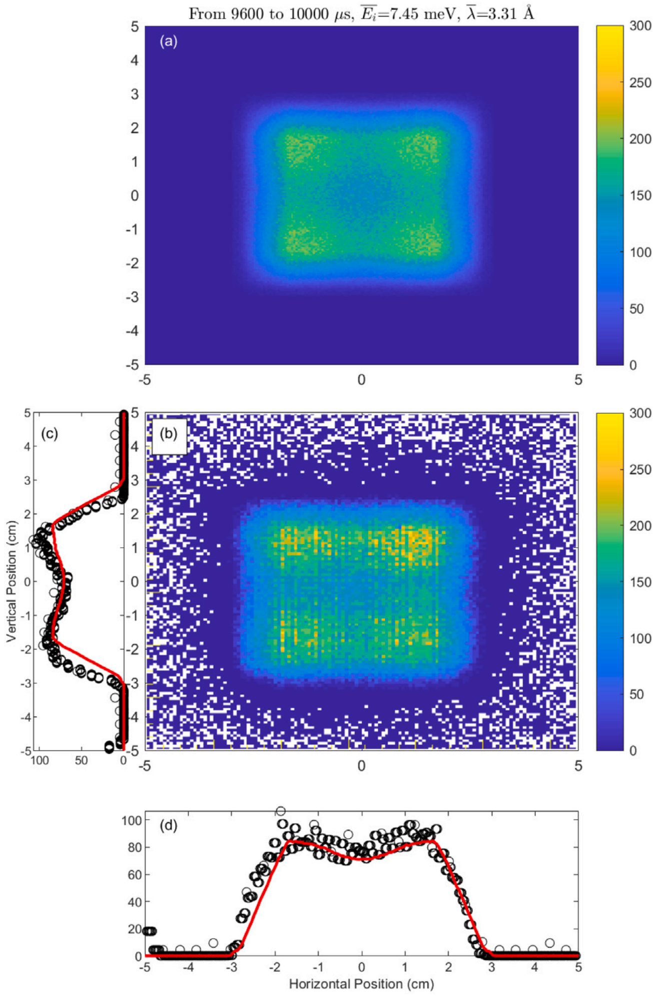

Fig. 4. MARI beam-profile after the upgrade, as calculated using McStas (a) and measured with a 2D (nGEM) detector at the sample position (b), together with the vertical (c) and horizontal (d) beam profiles. The nGEM measurements and McStas calculated profiles are both in arbitrary units and have been scaled to match each other.

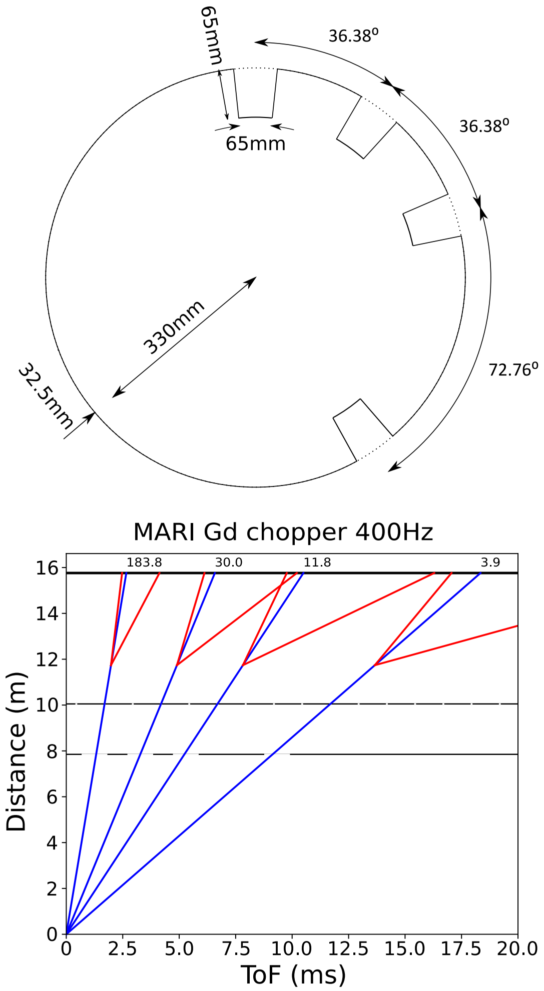

Fig. 5. The MARI disk chopper design and time–distance diagram for a representative configuration. Red lines denote the time range where inelastic scattering from a neutron energy gain of 300 K (left boundary) to a neutron energy loss of 90% of E_i (right boundary) would fall.

4. New disk chopper and RRM-mode

In addition to the new guide, MARI has also had a new counter-rotating double-disk chopper installed, which allows the repetition rate multiplication (RRM) technique to be used to measure multiple incident energy pulses simultaneously. RRM mode on MARI is designed to be used with the Fermi chopper running at 200, 400 or 600 Hz. For example at 400 Hz, every 2.5 ms the Fermi chopper will make a complete (2π) rotation, and hence transmit a pulse of neutrons. Thus 8 neutron pulses will be transmitted within the 20 ms window between proton pulses (a time "frame"). However, not all these pulses will be usable because the inelastic scattering from some of the pulses may overlap with other pulses.[2] To prevent this "pulse-overlap", the disk chopper has 4 slots designed to pass pulses corresponding to zero (the principal pulse), one ("2π"), two ("4π") or four ("8π") full rotations of the Fermi chopper at 400 Hz, as shown in Fig. 5. The curved boron chopper packages can only be used in RRM mode when run at 400 Hz, whilst the straight Gd chopper package is able to transmit a neutron pulse after half a rotation (a "π" pulse),[3] so may be used at 200 or 600 Hz as well. In addition, the two disk choppers may be phased to transmit a single or pairs of neutron pulses per proton pulse rather than all four, to allow more flexibility in operations. Transmitting a single pulse offers a lower background at the cost of being able to measure less, whilst transmitting two pulses (either the principal and "2π" or the principal and "4π" pulses at 400 Hz) may help with avoiding pulse-overlap.

5. Detector electronics upgrade

Concurrent with the guide upgrade, the detector electronics (but not the ^{3}He detector tubes) were upgraded. This consisted of new pre-amps, analogue-to-digital converters (ADC) and data-acquisition electronics (DAE).

Previously each tube on MARI was directly connected to its own pre-amp, housed in its own box, which was glued to the end of the tube. This meant that replacing faulty units took significant time and effort,

---

[2] The pulse overlap is dependent on the incident energy E_i of the pulse and chopper frequency but is negligible for E_i larger than ≈80 meV; for a Fermi frequency of 400 Hz, it could be up to 10% of E_i for $20 < E_i < 80$ meV and up to 25% for $10 < E_i < 20$; these overlaps will be larger for faster frequencies.

[3] Whilst a half-rotation"π"-pulse is transmitted by the sloppy chopper its transmission is reduced by a factor of ≈5 compared to the full rotation pulses so is usually not feasible to use.

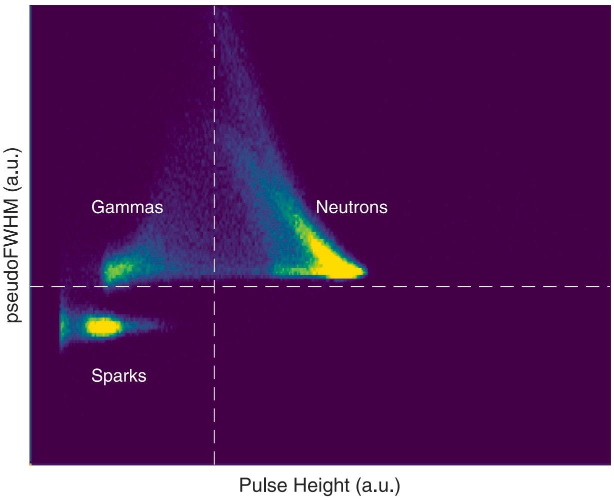

Fig. 6. Histogram of pseudoFWHM vs pulse-height computed from traces collected using an Acqiris digitizer, showing how neutron signals can be distinguished from signals from gamma radiation and electrical noise ("sparks").

and could only be done during a beam-off period. To ease maintenance we decided to replace this with PCB-mounted pre-amps where the pre-amps for sets of eight tubes are housed in a single box. Each PCB contains sixteen pre-amps so that a tube could be switched using a relay between one of two pre-amps in case of failure during a cycle. In addition each pre-amp box also houses environmental sensors for ambient temperature and humidity to enable preemptive maintenance should high temperatures or humidity be detected.

The new design, however, requires a short length of wire to connect the tubes to the new pre-amp which was not needed in the old design. During commissioning, it was discovered that the thin (3.1 mm diameter) standard copper wire used for this was prone to sparking which introduced large electrical background signals that can be mistaken for neutron counts by the DAE. The thin wire was originally chosen because they would need minimal modification of the ends of the tube as this only permitted a relatively small diameter wire. To solve this issue, we pursued two separate approaches: we investigated alternative wires for the link, and attempted to electronically distinguish the spark signal from neutron (or gamma) signals. The second approach was only possible because the new ADC is built around a field-programmable gate array (FPGA) which allows fast digital signal processing to be carried out within the unit and easy and fast updating of this firmware by "flashing" the unit. In the end, both methods for handling sparks were implemented: the thin wire was replaced by a much thicker (5.7 mm diameter) silicone-rubber sheathed high-voltage wire with the tube connectors re-designed and also a spark-rejection algorithm was incorporated into the ADC.

We now briefly discuss the spark-rejection algorithm, which relies on the spark signal being much more transient (shorter duration) than the response of the tube to ionization by neutrons or gammas. With the FPGA, we can compute a "pseudoFWHM" of the time response of the signal as:

$$\text{pseudoFWHM} = -V_0 \Bigg/ \left(\left. \frac{\partial^2 V}{\partial t^2} \right|_{t=t_0} \right) \tag{1}$$

where V_0 is the peak amplitude of the pulse and t_0 is the time of the center of the peak. This quantity is actually proportional to the square of the full width at half maximum if the signal is a Gaussian. We ensure that the signal is close to Gaussian by applying low-pass filters before computing the "pseudoFWHM", and avoid the costly square root computation which we found had little effect on the ability to discriminate sparks from other signals. The second derivative at the peak center is computed by finite difference of the digitized signal.

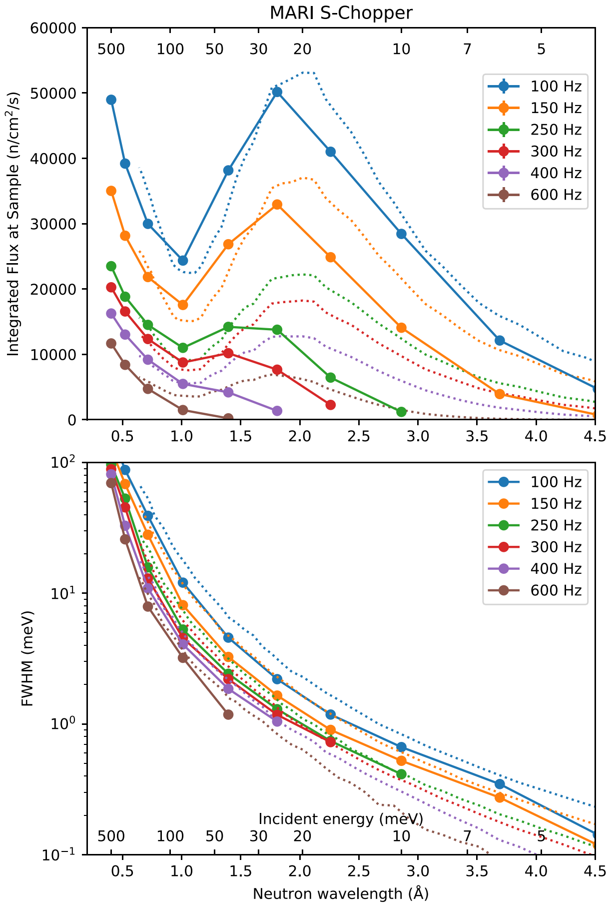

Fig. 7. Measured (solid lines and circles) flux and linewidth (FWHM) at the sample and calculated (dashed lines) flux and linewidth (FWHM) with the boron S chopper. The calculated flux has been scaled to match the peak experimental flux.

Fig. 6 shows an example 2D histogram of the signal amplitude vs "pseudoFWHM". The figure shows we can introduce two thresholds: a lower pulse-height threshold below which signals are considered to be gammas, and a lower pseudoFWHM threshold below which signals are considered to be sparks. Both thresholds were found to be necessary during operation of the instrument to obtain the true neutron events and eliminate the electrical background, despite most spark signals having low amplitudes which could be removed using just the pulse-height threshold.

6. Instrument performance

In order to verify the performance of the spectrometer after the upgrade, we performed extensive measurements with a standard annular vanadium sample. From this the integrated flux at a given incident energy and chopper frequency could be determined from the measured counts using the known sample mass and cross-sections.[4] Figs. 7 and

---

[4] The vanadium sample we used was an annulus of inner diameter 38 mm and outer diameter 40 mm and length 40 mm with a mass of 32.6 g. To determine the flux we calculate the number of neutrons scattered (n) from the standard sample by summing the counts in the detectors dividing by the time of measurement and the fractional detector solid area (fraction of 4π steradian). Then the flux is calculated from this divided by the scattering probability ($p = 1 - \exp(-N\sigma_s t)$ where N is the vanadium number density, $t = 4$ mm is the vanadium sample thickness and σ_s is the scattering cross-section of vanadium) and the area of the vanadium sample ($A = 16$ cm^2), giving $F = n/(pA)$ in neutrons/cm^2/s.

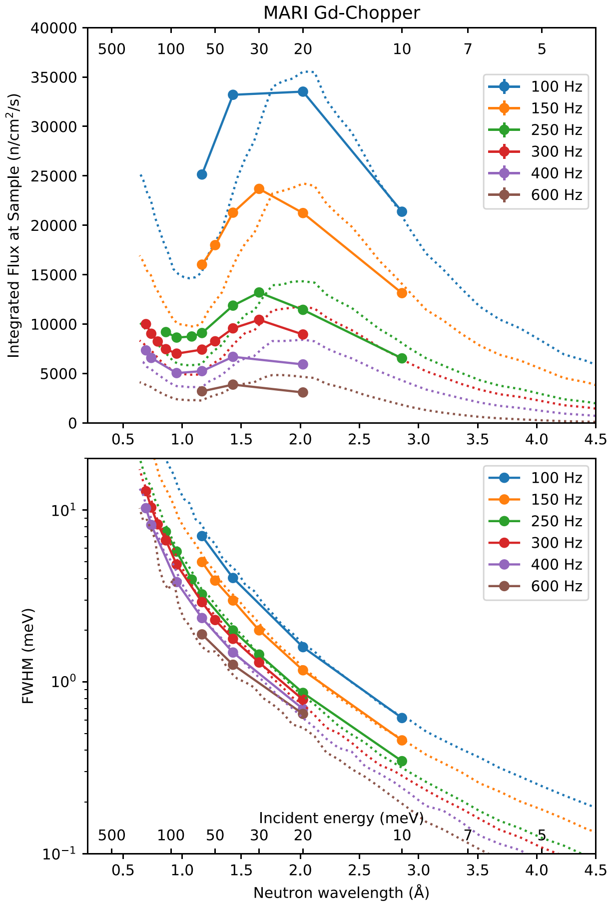

Fig. 8. Measured (solid lines and circles) flux and linewidth (FWHM) at the sample and calculated (dashed lines) flux and linewidth (FWHM) with the gadolinium chopper. The calculated flux has been scaled to match the peak experimental flux.

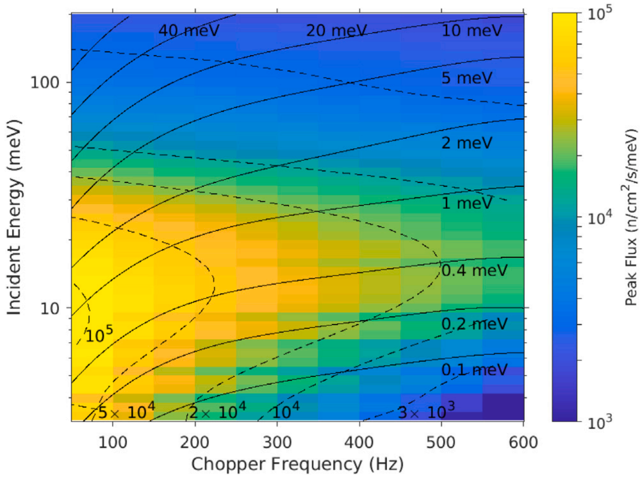

Fig. 9. Energy resolution at the detector (solid contours) and peak flux at the sample position (colormap and dashed contours) with the Gd chopper on MARI, from McStas simulations.

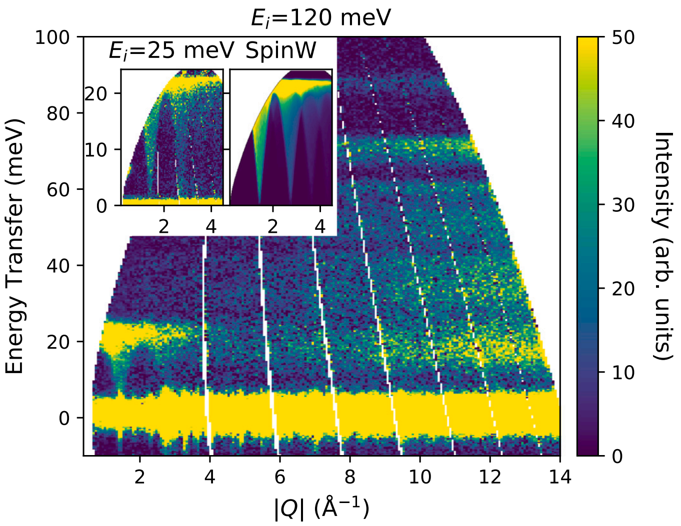

Fig. 10. Inelastic neutron spectra of $YCrO_3$ at 5 K with the empty sample container background subtracted. The inset shows the second "rep" at a lower incident energy which reveals details of the spin wave excitations confronted by a model linear spin wave calculation as described by Bajaj et al. [9].

8 show the measured and calculated integrated flux at the sample and vanadium elastic linewidths for the boron "S" (denoting medium or "Sloppy" resolution) and gadolinium choppers respectively. The calculated flux was obtained from McStas simulations by summing the simulated counts in a 1 cm × 1 cm wavelength monitor at the sample position. As noted above, we had to rescale the simulations to match the experimental measurements because due to inaccuracies in the MCNPX calculations which went into the moderator component, the simulated flux was a factor of ≈2 larger than the measurements.

Fig. 9 shows the (calculated) expected performance of MARI with the gadolinium chopper in an "at-a-glance" format, including both the *calculated* energy resolution and *calculated* peak flux as a function of incident energy and chopper frequency simultaneously, with contours indicating the resolution and colors the flux.

Compared to before the upgrade, we found that the energy resolution has become somewhat coarser due to the increased divergence from the guide, and from viewing a larger area of the moderator. We observed this effect to be more pronounced for low chopper frequencies, with the resolution being up to 50% broader compared to before the upgrade for the Gd chopper at $f = 100$ Hz, whereas for $f = 400$ Hz the broadening is only ≈10%. As most measurements now tend to use the higher frequencies, this has not seriously adversely affected operations of the instrument.

Finally, we observed no significant changes in the instrument background, except at low scattering angles due to the increased beam divergence.

7. Science highlights

Since the instrument was recommissioned in 2018, over 90 experiments have been carried out on MARI (including short "Xpress" experiments to characterize new samples). About two-thirds of these experiments are on magnetic materials, of which half are measurements of ordered spin waves, one third are crystalline electric field measurements and the remainder are on disordered systems, or magnetic clusters.

MARI's wide angular coverage ($5° < 2\theta <= 135°$) and ability to use repetition rate multiplication to measure several incident energies together is useful for simultaneous measurements of phonons and magnons, as exemplified by a recent work on the multiferroic material $YCrO_3$ [9]. Fig. 10 shows a single 3 h measurement with the Gd chopper running at 400 Hz that captures data at both $E_i = 120$ meV and $E_i = 25$ meV. The $E_i = 120$ meV data clearly shows the phonon modes at high $|Q|$, whilst the $E_i = 25$ meV pulse shows details of the spin wave spectrum which can now be readily modeled with programs such as `SpinW` [10].

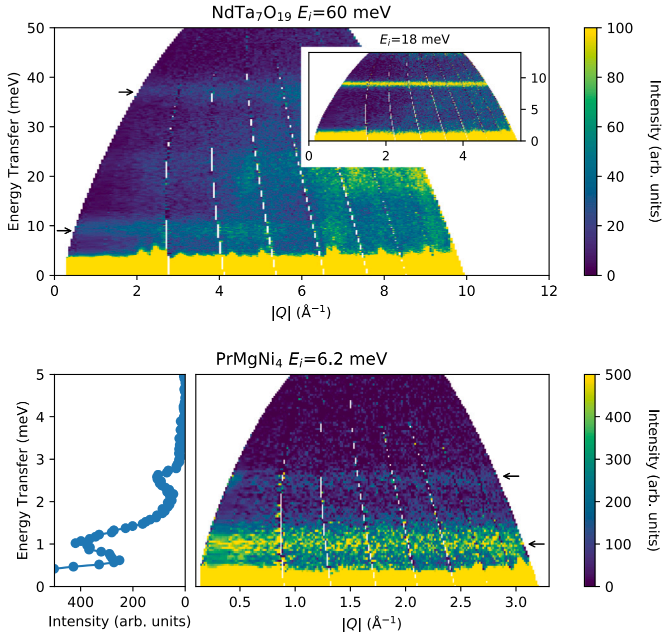

Fig. 11. Inelastic neutron spectra of (top) $NdTa_7O_{19}$ at 5 K with E_i = 60 meV and (top inset) E_i = 18 meV, and (bottom) $PrMgNi_4$ showing crystalline electric field transitions as indicated by the arrows. The scattering around 20 meV at high $|Q|$ in the $NdTa_7O_{19}$ E_i = 60 meV data is from Aluminum phonons from the sample container. (Bottom left) A line cut integrated over the range $0 < |Q| < 2$ Å^{-1} showing crystalline electric field excitations at 1 and 2.6 meV in $PrMgNi_4$.

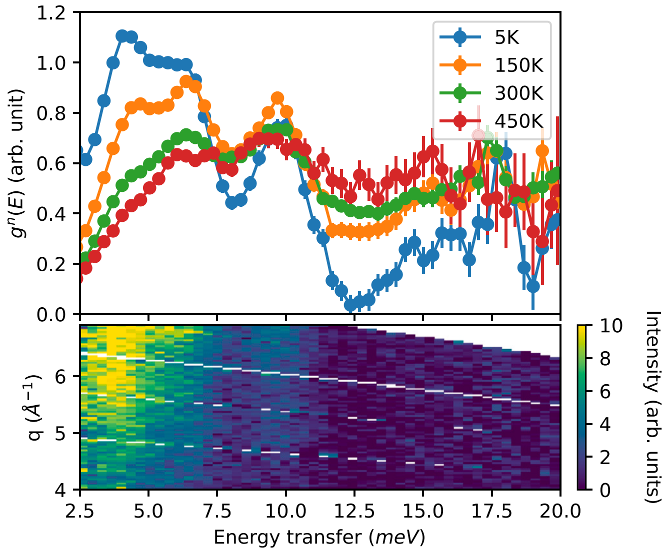

Fig. 12. Neutron weighted phonon density of state $g^n(E)$ as a function of temperature (upper panel) and powder inelastic neutron spectra (lower panel) of $TlInTe_2$ at 5 K.

Crystalline electric field (CEF) measurements account for a significant amount of beam time on MARI, with measurements on traditional strongly correlated intermetallics such as $PrMgNi_4$ [11] and on newer geometrically frustrated oxides such as the quantum spin-liquid candidate $NdTa_7O_{19}$ [12], both shown in Fig. 11.

In the case of $PrMgNi_4$, the cubic point group is expected to split the $J = 4$ ground multiplet into two triplets, a doublet and a singlet, with the Γ_3 doublet being the ground state, and yielding two dipole allowed transitions at the lowest temperatures. Instead, the experiment observed three transitions, at 11.6 (not shown), 2.5 and 1.1 meV. These two lower energy transitions indicate a splitting of the Γ_3 doublet, likely due to a symmetry lowering caused by Pr-Mg inter-site disorder, which in turn prevents a quadrupolar ordering seen in similar cubic praseodymium intermetallics [11]. Prior to the upgrade, MARI would have struggled to measure the 1.1 meV level as we would have needed to use higher incident energies with worse resolution. The increased flux at lower energies from the guide upgrade instead allowed us to use a lower incident energy and to thus clearly resolve the mode.

$NdTa_7O_{19}$ is a triangular lattice antiferromagnet and quantum spin liquid candidate where no magnetic order has been observed above 66 mK. Crucially it shows no evidence of the site disorder that complicates other spin liquid candidates. Neutron scattering measurements and fits of the Nd crystal fields reveal a strong Ising anisotropy in agreement with ESR data, but with some residual xy character. The dominant Ising anisotropy together with the triangular geometry is thought to prevent magnetic ordering, whilst the residual xy interactions acts as a perturbing transverse field which could lead to a zero temperature phase transition [12].

Finally, although magnetic studies have been a staple of experiments on MARI historically, a rising proportion of experiments are now looking at phonons in functional materials, such as batteries cathode materials, ionic conductors or thermoelectrics. One recent example is the Zintl phase $TlInTe_2$ [13], whose INS spectrum and neutron-weighted phonon density of states (PDOS) is shown in Fig. 12. This potential thermoelectric material has an ultra-low thermal conductivity, ≈0.4 W m^{-1} K^{-1} above room temperature. Measurements on MARI together with an X-ray pair distribution function study showed that this is due to highly anharmonic rattling of Tl ions inside $InTe_2$ cages which causes strong phonon scattering and hence strongly suppresses the thermal conductivity. The rattling is anisotropic and leads to several low energy modes which can be seen at around 3.5, 5.6 and 9.5 meV in Fig. 12 which broaden dramatically as the temperature rises confirming their anharmonicity.

8. Summary

The MARI spectrometer at ISIS has been upgraded with new $m = 3$ supermirror guides giving a factor of 6 gain in flux at $\lambda = 1.8$ Å (E = 25 meV) where the peak flux from the methane moderator is, whilst larger gains at lower energies enable new measurements which were previously unfeasible.

The detector electronics were also upgraded with a new FPGA-based ADC to allow fast and flexible digital signal processing.

Finally, the upgrade also includes a new double disk chopper which allows routine use of repetition rate multiplication without rep-overlap to improve experimental throughput. For example the full dispersion bandwidths of phonon or magnon excitations can be measured by one incident energy neutron pulse whilst details of the dispersion or possible energy gaps can be probed simultaneously with another incident energy pulse.

The upgrades have together allowed MARI to continue to deliver a high quality science program well into its fourth decade, covering a wide range of topics from quantum magnetism to functional materials.

Declaration of competing interest

The authors declare that they have no known competing financial interests or personal relationships that could have appeared to influence the work reported in this paper.

Data availability

The data will be made available on Zenodo.

Acknowledgments

The guide and detector electronics upgrade of MARI was made possible thanks to the efforts of numerous ISIS staff involved in various aspects of the project. We are grateful for their effort and support that enabled the project to be completed successfully.

Appendix A. Supplementary material

https://doi.org/10.5281/zenodo.8314687

References

[1] A.D. Taylor, M. Arai, S.M. Bennington, Z.A. Bowden, R. Osborn, K. Andersen, W.G. Stirling, T. Nakane, K. Yamada, D. Welz, Proc. ICANS-XI, KEK, Tsukuba, 1990, pp. 705–710.

[2] K. Andersen, Nucl. Instrum. Methods Phys. Res. A 371 (3) (1996) 472–479.

[3] K.H. Andersen, M. Bertelsen, L. Zanini, E.B. Klinkby, T. Schönfeldt, P.M. Bentley, J. Saroun, J. Appl. Crystallogr. 51 (2) (2018) 264–281.

[4] R. Bewley, D. Pooley, Nucl. Instrum. Methods Phys. Res. A 1039 (2022) 167161.

[5] P.K. Willendrup, K. Lefmann, J. Neutron Res. 22 (2020) 1–16.

[6] G. Škoro, S. Lilley, R. Bewley, Physica B 551 (2018) 381–385, The 11th International Conference on Neutron Scattering (ICNS 2017).

[7] H. Ohshita, M. Ishiwata, K. Iwase, F. Fujisaki, S. Muto, S. Satoh, T. Seya, M. Sakaguchi, T. Otomo, K. Ikeda, N. Kaneko, K. Suzuya, Proceedings of the 2nd International Symposium on Science At J-PARC — Unlocking the Mysteries of Life, Matter and the Universe —.

[8] R. Ewings, A. Buts, M. Le, J. Van Duijn, I. Bustinduy, T. Perring, Nucl. Instrum. Methods Phys. Res. A 834 (2016) 132–142.

[9] N. Bajaj, A.P. Roy, A. Khandelwal, M.K. Chattopadhyay, V. Sathe, S.K. Mishra, R. Mittal, P.D. Babu, M.D. Le, J.L. Niedziela, D. Bansal, J. Phys.: Condens. Matter 33 (12) (2021) 125702.

[10] S. Toth, B. Lake, J. Phys.: Condens. Matter 27 (16) (2015) 166002.

[11] Y. Kusanose, T. Onimaru, Y. Yamane, K. Umeo, T. Takabatake, T. Guidi, D. Le, D. Adroja, J. Phys. Conf. Ser. 2164 (1) (2022) 012052.

[12] T. Arh, B. Sana, M. Pregelj, P. Khuntia, Z. Jagličić, M.D. Le, P.K. Biswas, P. Manuel, L. Mangin-Thro, A. Ozarowski, A. Zorko, Nature Mater. 21 (2022) 416–422.

[13] M. Dutta, M. Samanta, T. Ghosh, D.J. Voneshen, K. Biswas, Angew. Chem., Int. Ed. 60 (8) (2021) 4259–4265.